

## AN EXTERNAL SHOCK ORIGIN OF GRB 141028A

J. MICHAEL BURGESS<sup>1,2,†</sup>, DAMIEN BÉGUÉ<sup>1,2,‡</sup>, FELIX RYDE<sup>1,2</sup>, NICOLA OMODEI<sup>3</sup>, ASAF PE'ER<sup>4</sup>, J. L. RACUSIN<sup>5</sup>,  
A. CUCCHIARA<sup>5</sup>

*Draft version September 24, 2018*

### ABSTRACT

The prompt emission of the long, smooth, and single-pulsed gamma-ray burst, GRB 141028A, is analyzed under the guise of an external shock model. First, we fit the  $\gamma$ -ray spectrum with a two-component photon model, namely synchrotron+blackbody, and then fit the recovered evolution of the synchrotron  $\nu F_\nu$  peak to an analytic model derived considering the emission of a relativistic blast-wave expanding into an external medium. The prediction of the model for the  $\nu F_\nu$  peak evolution matches well with the observations. We observe the blast-wave transitioning into the deceleration phase. Further we assume the expansion of the blast-wave to be nearly adiabatic, motivated by the low magnetic field deduced from the observations. This allows us to recover within an order of magnitude the flux density at the  $\nu F_\nu$  peak, which is remarkable considering the simplicity of the analytic model. Across all wavelengths, synchrotron emission from a single forward shock provides a sufficient solution for the observations. Under this scenario we argue that the distinction between *prompt* and *afterglow* emission is superfluous as both early and late time emission emanate from the same source. While the external shock model is clearly not a universal solution, this analysis opens the possibility that at least some fraction of GRBs can be explained with an external shock origin of their prompt phase.

*Subject headings:* gamma-ray burst: individual (141028A) – radiation mechanisms: non-thermal – radiation mechanisms: thermal

### 1. INTRODUCTION

Identifying the origin of the dynamical evolution of gamma-ray burst (GRB) outflows is an unsolved issue, critical to the understanding of both the energetics and spectra of these events. One idea is that the emission is the result of synchrotron radiation from an external forward shock propagating into the external circumburst medium (CBM) (Cavallo & Rees 1978; Rees & Mészáros 1992; Mészáros & Rees 1993; Chiang & Dermer 1999; Dermer et al. 1999; Dermer & Mitman 1999). This mechanism should produce smooth  $\gamma$ -ray pulses with durations on the order of a few seconds for typical GRB parameters. However, the short-time variability (on the order of a few milliseconds) of many GRB light curves ruled out this postulate as a universal mechanism (e.g. Sari & Piran 1997; Kobayashi et al. 1997; Walker et al. 2000) and gave favor to several alternative hypotheses including models that consist of rapid internal shocks in an unsteady outflow (Rees & Mészáros 1994) or magnetic reconnection (e.g., Spruit et al. 2001; Drenkhahn & Spruit 2002; Zhang & Yan 2011) to account for the observed emission.

Still, there do exist long and temporally smooth GRBs with typical variability time scales larger than a few seconds (see Golkhou & Butler 2014; Golkhou et al. 2015) that do not violate the variability constraints of the external shock model and can be tested via their spectral evolution as to whether they conform to the well-established predictions made by this model. The simplicity of the model affords it the ability to be tested both spectrally and temporally, a feature unique to the external shock model. The dynamics and spectra of the internal shock model have been simulated (Daigne & Mochkovitch 1998), but the dynamics rely on assumed and degenerate configurations from variations in the wind (e.g. the radial distribution of the Lorentz factors), forbidding the formulation of unique predictions that can be identified in the data. Therefore, it is currently impossible to test the internal shock model in the manner presented here without severe degeneracies. Additionally, the internal shock model has trouble efficiently converting the internal kinetic energy of a GRB into radiation, which is challenging when trying to explain the extreme luminosities observed (Kobayashi et al. 1997).

Herein, we analyze the bright, long, single-pulsed GRB 141028A and find several clues for an external shock origin of its emission. We fit the GRB's time-resolved spectra with a slow-cooled synchrotron+blackbody model (Burgess et al. 2014b) and examine the evolution of the spectra. The evolution of the synchrotron  $\nu F_\nu$  peak ( $E_p$ ) is fit with an analytic physical model predicted by Dermer et al. (1999). From this fit, we obtain physical parameters such as the coasting Lorentz factor and CBM radial profile which can then be used to predict how the flux of the prompt emission should evolve. Comparing these predictions to the data

<sup>1</sup> The Oskar Klein Centre for Cosmoparticle Physics, AlbaNova, SE-106 91 Stockholm, Sweden

<sup>2</sup> Department of Physics, KTH Royal Institute of Technology, AlbaNova University Center, SE-106 91 Stockholm, Sweden

<sup>†</sup> jamesb@kth.se

<sup>‡</sup> damienb@kth.se

<sup>3</sup> W. W. Hansen Experimental Physics Laboratory, Kavli Institute for Particle Astrophysics and Cosmology, Department of Physics and SLAC National Accelerator Laboratory, Stanford University, Stanford, CA 94305, USA.

<sup>4</sup> Physics Department, University College Cork, Cork, Ireland

<sup>5</sup> NASA Goddard Space Flight Center, Greenbelt, MD 20771, USA

enables us to test the validity of the model in several ways.

The article is organized in the following manner. In Section 2, we introduce the formalism of the external shock model to derive a function for  $E_p(t)$  to fit to data. In Section 3, the observations and spectral analysis are introduced. Section 4 details our application of the external shock model to the data. The parameters resulting from the analysis are used to make further predictions regarding the flux evolution of the prompt phase of the GRB. From there, we analyze the photospheric emission. In Sections 5.1 and 5.2, we discuss the compatibility of our results with the high and low-energy late-time observations.

## 2. THE EXTERNAL SHOCK MODEL

The external shock model is built upon the blast-wave evolution derived in Blandford & McKee (1976) which tracks the evolution of a relativistically expanding fireball into an external medium. The equations can be applied to GRBs by assuming some fraction of the electrons in the shocked external medium is accelerated to high energies by the shock wave and radiates a fraction of the kinetic energy away via synchrotron radiation (Cavallo & Rees 1978; Rees & Mészáros 1992). In this work, we use the analytic formalism developed in Dermer et al. (1999) to fit the spectral evolution of the emission. We briefly review the main equations required and refer the reader to Dermer et al. (1999); Chiang & Dermer (1999) for more details on the model.

The blast-wave is assumed to expand into an external circumburst medium (CBM) with a radial density evolution modeled as a power law,

$$n(x) = n_0 x^{-\eta} \text{ cm}^{-3} \quad (1)$$

where  $n_0$  is the initial density and  $\eta$  describes the radial morphology of the CBM such that  $\eta = 0$  is a constant density and  $\eta = 2$  describes a stellar wind. The dimensionless radial coordinate is  $x = r/r_d$  where, following the convention that a quantity  $w = w_n 10^n$ ,

$$r_d = 5.4 \cdot 10^{16} \left[ \frac{(1 - \eta/3) E_{0,54}}{n_{0,2} \Gamma_{0,2}^2} \right]^{1/3} \text{ cm} \quad (2)$$

is the radius at which the blast has swept up a significant amount of mass ( $\propto \Gamma^{-1}$ ) to begin decelerating (Rees & Mészáros 1992). Following the solution of Blandford & McKee (1976) the evolution of the bulk Lorentz factor ( $\Gamma$ ) of the blast-wave is modeled as a broken power law consisting of a coasting phase followed by a deceleration phase:

$$\Gamma(x) = \begin{cases} \Gamma_0 & x < 1 \\ \Gamma_0 x^{-g} & 1 \leq x \end{cases} \quad (3)$$

where  $\Gamma_0$  is the coasting Lorentz factor and  $g$  is the radiative regime index. For a constant density ( $\eta = 0$ ) CBM,  $g = 3, 3/2$  indicate the fully radiative and non-radiative (adiabatic) expansion regimes respectively (Blandford & McKee 1976). A fraction of the blast energy is dissipated in the shock and accelerates electrons to high energies, which subsequently radiate this away via synchrotron radiation. Following the parameterization of Dermer et al.

(1999), the temporal evolution of the  $\nu F_\nu$  peak energy,  $E_p$ , of this synchrotron radiation can be modeled as

$$E_p(t) = \mathcal{E}_0 \left[ \frac{\Gamma(x)}{\Gamma_0} \right]^4 x^{-\eta/2} \text{ keV} \quad (4)$$

where

$$\mathcal{E}_0 = 15 \frac{n_{0,2}^{1/2} q_{-3} \Gamma_{0,2}^4}{1+z} \text{ keV} \quad (5)$$

is the observed  $E_p$  at the observed deceleration time,

$$t_d = \frac{r_d}{\Gamma_0^2 c} (1+z). \quad (6)$$

Here,  $c$  is the speed of light and  $q$  parameterizes the magnetic field and shock acceleration microphysics such that  $q \equiv [\epsilon_B (r_s/4)]^{1/2} \epsilon_e^2$ . Here  $\epsilon_B$  and  $\epsilon_e$  are the magnetic and electron equipartition factors and  $r_s \simeq 4$  is the shock compression ratio. For values expected in GRBs and to coincide with our choice of slow-cooling synchrotron to fit the spectra, if we take  $\epsilon_B \simeq 10^{-4}$  and  $\epsilon_e \lesssim 0.5$  then we have values of  $q \simeq 10^{-3}$ . While these values of  $\epsilon_B$  are lower than the typically assumed values of  $\sim 10^{-2}$ , recent studies (Lemoine et al. 2013; Santana et al. 2014) find that the values can be much lower and we therefore follow these works. For the analysis, we will allow values  $\epsilon_B \lesssim 10^{-2}$  to cover the range of typically assumed values.

Additionally, we can write the measured  $\nu F_\nu$  peak luminosity as

$$P_p(t) = \Pi_0 \begin{cases} x^{2-\eta} & 0 \leq x < 1 \\ x^{2-\eta-4g} & 1 \leq x < \Gamma_0^{1/g} \end{cases} \quad (7)$$

where

$$\Pi_0 \propto \frac{(2g - 3 + \eta) m_p c^3 \Gamma_0^4 n_0 A_0}{2g(1+z)^2} \text{ erg s}^{-1}. \quad (8)$$

Here,  $m_p$  is the proton mass and  $A_0$  is the blast-wave area factor. The proportionality in Equation 8 comes from the fact that in Dermer et al. (1999) an empirical photon model is used to create light curves and here we will be using synchrotron emission directly to fit the time-resolved spectra of GRB *141028A* (see Section 3).

With these equations, the external shock model can predict several observable quantities, namely, the evolution of  $E_p$  and  $P_p$  which we test below in Section 4.2. The effects on the  $E_p$  evolution of different parameters is shown in Figure 1. The parameters have the following dominant effects:

- $\Gamma_0$ : sets the break time
- $\eta$ : sets the slope of early  $E_p$  decay
- $g$ : sets the slope of late  $E_p$  decay.

These parameters, along with  $q$  which acts as a normalization, will be the free parameters that will be determined by fitting the observed evolution of  $E_p$  to Equation 4. In reality, the range of values for  $g$  are determined by the value of  $\eta$  (Dermer et al. 1999). Since we cannot know a priori the value of  $\eta$ , we treat  $g$  as an independent parameter. It is important to note that this analytic approximation to the blast-wave evolution fails to capture some aspects that the full numerical solution exhibits

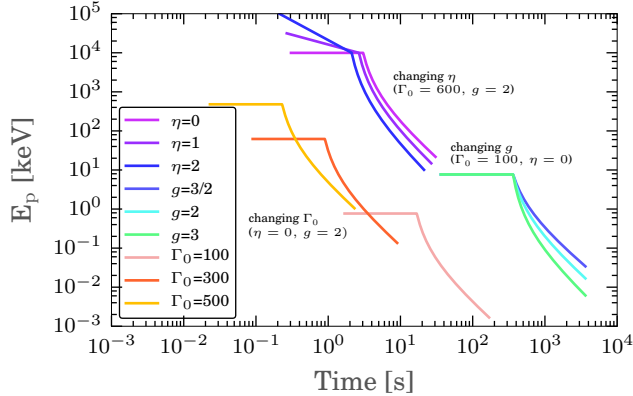


**Figure 1.** Demonstrating the effect of the physical parameters on the evolution of  $E_p$  with time. It is easy to see that  $\Gamma_0$  has the strongest effect on the timescale of the burst, while  $\eta$  affects the early evolution of  $E_p$  and  $g$  the late evolution.

(Chiang & Dermer 1999). Most notable is the smooth transition from coasting to decelerating at the deceleration radius ( $r_d$ ). The formalism we adopt will serve as a proof of concept that will be further applied to a larger sample and improved upon with a full numerical treatment.

### 3. OBSERVATIONS OF GRB 141028A

#### 3.1. Data Acquisition

Rapid variability poses a problem for the external shock model; therefore, bright, long, single-pulsed GRBs provide the most viable candidates for being produced by external shocks. GRB 141028A is an example of this class of GRB (see Figure 2). GRB 141028A was discovered by the *Fermi* Gamma-ray Burst Monitor (GBM) (Roberts 2014; Meegan et al. 2009) and the bright GRB triggered an autonomous repoint of the *Fermi* spacecraft to optimize the Large Area Telescope (LAT) (Atwood et al. 2009) for follow-up observations. In ground analysis, LAT also localized and detected the GRB (Bissaldi et al. 2014) until  $\sim 10^3$  s after the trigger. The localization led to a target of opportunity observation by the narrow-field *Swift* instruments (the X-ray Telescope, XRT; and the Ultraviolet Optical Telescope, UVOT) (Gehrels et al. 2004). The X-ray and optical afterglow was detected by XRT (Kennea 2014) and UVOT (Siegel & Pagani 2014), and subsequently by many different ground-based facilities, including a measurement of a redshift of  $z=2.332$  with the Very Large Telescope/X-Shooter instrument (Malesani 2014). We collected optical/NIR photometry from GCN circulars, and constructed a multi-band SED using GROND data (Kann 2014), and light curves using  $r'$  and  $i'$  filters (GROND, RATIR: Troja (2014), P60: Cenko (2014), LCOGTN: Kopac (2014)). The XRT light curve and spectra were obtained from the XRT Team Repository (Evans et al. 2007, 2009). We triggered a pre-approved late-time Chandra target of opportunity observation to constrain the properties of the break in the X-ray afterglow hinted at by XRT. The 40 ks Chandra observation was analyzed with CIAO v4.6, yielding a faint detection which was converted to flux using the fit to the XRT spectrum. The X-ray and optical afterglow observations began at  $\sim 10^4$  s after the GBM trigger. It is therefore impossible

to observe the continuous evolution of the flux from the prompt to afterglow phase at low-energy.

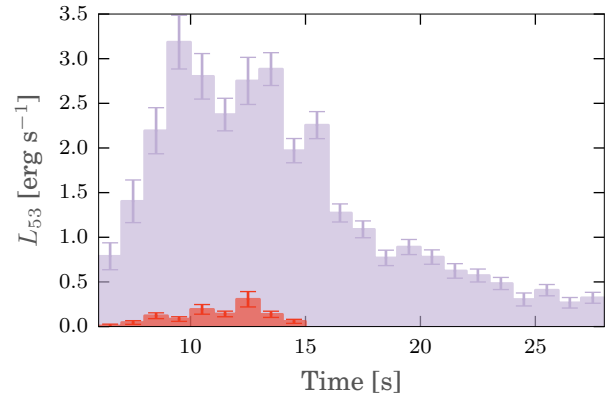


**Figure 2.** The luminosity lightcurve of GRB 141028A consisting of the synchrotron (purple) and blackbody (red) components.

#### 3.2. Spectral and Temporal Analysis

For the prompt emission, we use GBM time-tagged event (TTE) data and *Fermi* LAT low-energy (LLE) data to perform spectral analysis. The LLE technique is an analysis method designed to study bright transient phenomena in the 30 MeV - 1 GeV energy range, and was successfully applied to *Fermi*-LAT GRBs (Ackermann et al. 2013) and solar flares (Ackermann et al. 2012; Ajello et al. 2014). The idea behind LLE is to maximize the effective area below  $\sim 1$  GeV by relaxing the standard analysis requirement on background rejection. The first five seconds after the trigger time are excluded because the count rate was too low to constrain a spectral model.

Using the method of Gao et al. (2012), we calculated the variability components of GRB 141028A during the prompt emission. We find the dominant component to be  $t_{\text{var}} = 24.7/(1+z)$  s and an insignificant fast component with  $t_{\text{var}} = 3.8/(1+z)$  s. These values place the burst safely within the range of what can be expected by an external shock. We use time bins of 1 s to be sure to bin below the fast variability component. To fit the time-resolved spectra, we employ a two-component model consisting of synchrotron emission from an incompletely cooled electron distribution (slow-cooled) and a blackbody (Burgess et al. 2011, 2014b) (see Figure 3). In Burgess et al. (2014b), it was shown that single pulsed GRBs have spectra that are compatible with slow-cooled synchrotron sometimes with and sometimes without the addition of a blackbody. This motivates our choice of the synchrotron+blackbody photon model for fitting the spectra of the GRB 141028A. We note that not all GRB spectra are compatible with this photon model. There exist GRBs such as GRB 090902B with a clear dominant photospheric component originating from subphotospheric dissipation (Pe'er et al. 2005; Ryde et al. 2010).

The synchrotron model implemented is fully physical in the sense that the spectral shape comes from the synchrotron emissivity and electron distribution alone. The spectral fitting *should not* be confused with fitting the empirical Band function (Band et al. 1993) with its vari-

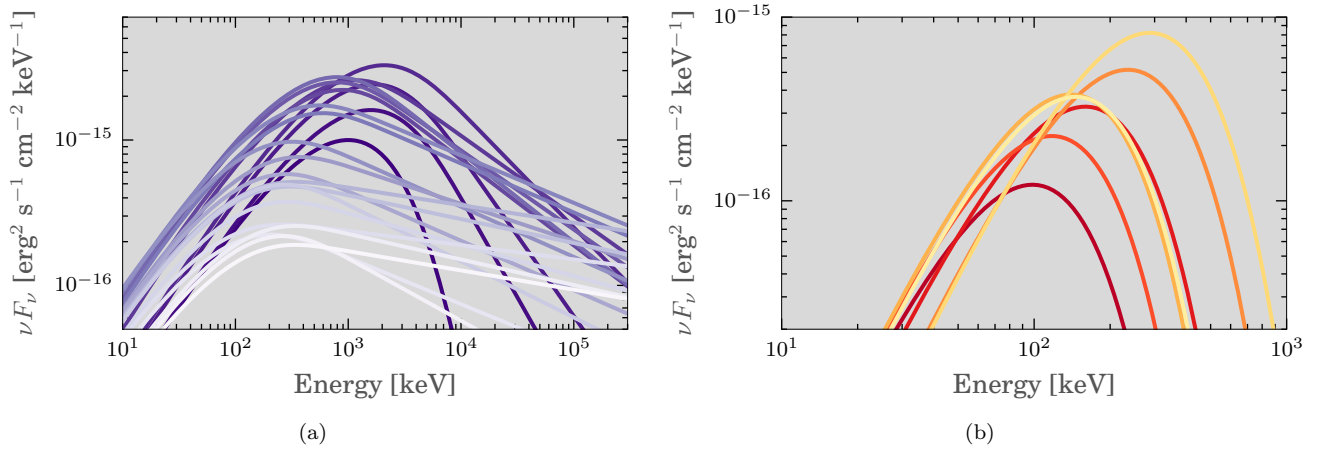


**Figure 3.** The time-resolved  $\nu F_\nu$  spectra in 1 s intervals of the synchrotron (5-27 s) (a) and blackbody (5-15 s) (b) components from the GBM+LLE fits. The synchrotron spectrum evolves in time from *purple* to *white* while the blackbody evolves from *red* to *yellow*.

able low-energy index ( $\alpha$ ). The blackbody is only included in time bins that statistically require it via a likelihood ratio test. We find that this statistical requirement produces a continuous presence of the blackbody for the first part of the observation. The data are well fit by the two-component model (see Table 1 for a summary of the spectral fits) and we observe two key features that motivate our investigation of the GRB under the framework of the external shock model:  $E_p$  evolves as a broken power law in time and the blackbody is only significant for a duration of  $\sim 10$  seconds compared to the total prompt duration of  $\sim 25$  s (see Section 4.4).

We calculate the total k-corrected energy (Hogg et al. 2002) in the synchrotron component in the 30 keV-300 MeV interval by summation over each time bin:  $E_{\text{SYNCH}} = 4\pi d_L^2 \sum F^{\text{SYNCH}} \Delta t_i \sim 9.1 \cdot 10^{53}$  erg. The total isotropic energy of the burst is estimated to be several times larger. In the following, we take the total isotropic energy (kinetic + radiative) of the blast-wave to be  $E_{\text{iso}} \cong 10^{55}$  erg while noting that this is an extremely high value. Nevertheless, the GRB is extremely bright and no mechanism is known that is efficient enough to convert the entire rest mass of the progenitor to radiation.

For the late time GeV emission, we performed an unbinned likelihood analysis of the LAT data to recover the energy flux ( $F_E$ ) and photon index ( $\gamma_{\text{ph}}$ ) of the emission (see Table 2) with the `gtlike` program distributed with the `Fermi ScienceTools`<sup>8</sup>. We selected P7REP\_SOURCE\_V15 photon events from a  $15^\circ$  circular region centered at the Swift XRT position (R.A.=322:60, Dec.=−0:23, J2000) and within  $105^\circ$  from the local zenith (to reduce contamination from the Earth limb). Events with measured energy from 100 MeV to 10 GeV are included in our analysis (the highest energy event associated with this GRB has an energy of 3.8 GeV and arrives 157.5 seconds after the GBM trigger time). Further details on the LAT analysis are discussed in Appendix A.

#### 4. EXTERNAL SHOCK ANALYSIS

##### 4.1. $E_p$ Evolution

After performing spectral fits to the data we can test the external shock model by fitting the evolution of the recovered synchrotron  $E_p$  with Equation 4. The fit is performed with a Bayesian analysis tool built upon the MULTINEST (Feroz et al. 2009) software which allows us to fully explore the correlated parameter space of the model. The free parameters in the fit are  $\Gamma_0$ ,  $\eta$ ,  $g$ , and  $q_{-3}$  to which we assign flat priors that are consistent with physical expectations ( $\Gamma_0 \in \{10, 1500\}$ ,  $\eta \in \{0, 2\}$ ,  $g \in \{0, 3\}$ ,  $q_{-3} \in \{0, 10\}$ ). We also note that it is not possible to fit for the density  $n_0$ , which we set at  $n_0 = \{1, 10, 100\} \text{ cm}^{-3}$  with different values mainly affecting the value of  $\Gamma_0$  recovered. Calculations in the text and figures assume  $n_0 = 100 \text{ cm}^{-3}$  but are complemented with calculations at the other values in associated tables. Figure 4 shows the fit of the  $E_p$  evolution and the best-fit parameters are detailed in Table 3.

We find that  $g \simeq 1.3$ , which is less than what is expected if the blast-wave decelerates adiabatically ( $g = 1.5$ ). This suggests that the blast-wave is still transitioning to the asymptotic limits of Equation 3. To test this

<sup>8</sup> We used version 09-34-02 available from the *Fermi* Science Support Center <http://fermi.gsfc.nasa.gov/ssc/>

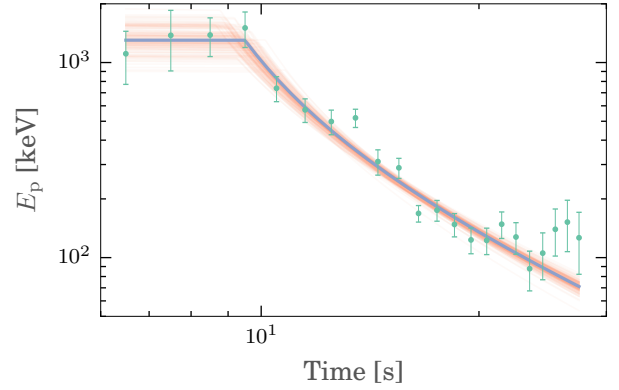


**Figure 4.** Bayesian fit of the  $E_p$  evolution of GRB 141028A. The maximum-likelihood point is indicated by the *blue* curve and posterior samples are in *orange*. The fitted parameters are indicated in Table 3.

assumption, we numerically solved for the evolution of  $\Gamma$  with radius via the equations of energy and momentum conservation and examined the transition phase in Figure 5. There is clearly a region that corresponds to our recovered value of  $g \simeq 1.3$ . Late (hundreds of seconds after the trigger) time observations smoothly connecting the prompt and afterglow emission would allow us to measure the asymptotic value of  $g$ . Yet, with the recovered fit parameters, we can calculate several physical properties of the outflow including  $r_d = 3.4 \cdot 10^{16}$  cm and the resulting predicted  $P_p(t)$  evolution though we will assume  $g \simeq 1.6$  to calculate fluxes as this is the value reached asymptotically in the near adiabatic case Chiang & Dermer (1999). These parameter values are used in the following sections to gain more insight about the GRB and its surrounding environment.

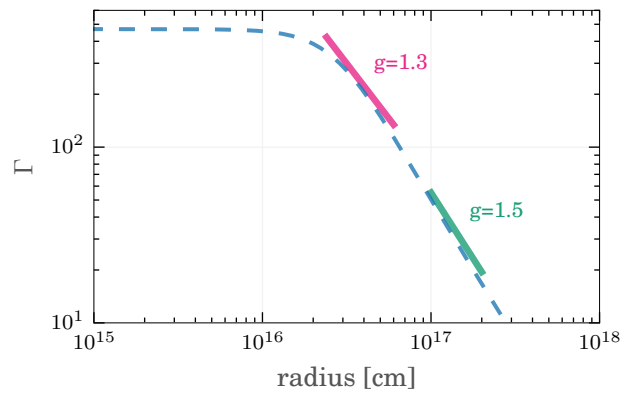


**Figure 5.** The blast-wave Lorentz factor evolution from our numerical simulation of the external shock model (*blue dashed line*). We illustrate that we are most likely finding the blast-wave still evolving in the transition phase, which accounts for the shallow value of  $g$  found in the fit of  $E_p$ .

##### 4.2. Peak Flux - $E_p$ plane

Using the recovered parameters from the fit, we can use Equations 4 and 7 to predict the evolution in the  $P_p$ - $E_p$  plane. In Figure 6, the data from GRB 141028A is plotted with the predicted curve from the external shock model derived from the  $E_p$  fits. Noting the discussion in Section 4.1, negative fluxes would be obtained

**Table 1**  
Results of the time-resolved spectral analysis of GBM+LLE data (10 keV - 300 MeV).

$T_{\text{start}}$ [s]	$T_{\text{stop}}$ [s]	$F_{\text{E}}^{\text{SYNCH}}$ [erg s $^{-1}$ ] <sup>b</sup>	$E_{\text{p}}$ [keV] <sup>c</sup>	$p^{\text{d}}$	$F_{\text{E}}^{\text{BB}}$ [erg s $^{-1}$ ]	$kT$ [keV]
6.0	7.0	$(1.79 \pm 0.34) \cdot 10^{-6}$	$1109 \pm 336$	10.00 <sup>a</sup>	$(1.61 \pm 3.43) \cdot 10^{-8}$	$24.55 \pm 26.48$
7.0	8.0	$(3.19 \pm 0.54) \cdot 10^{-6}$	$1378 \pm 472$	$5.74 \pm 1.21$	$(1.04 \pm 0.54) \cdot 10^{-7}$	$25.12 \pm 4.50$
8.0	9.0	$(4.99 \pm 0.59) \cdot 10^{-6}$	$1383 \pm 310$	$5.21 \pm 0.58$	$(2.76 \pm 0.59) \cdot 10^{-7}$	$40.69 \pm 5.40$
9.0	10.0	$(7.25 \pm 0.68) \cdot 10^{-6}$	$1504 \pm 310$	$4.59 \pm 0.30$	$(1.91 \pm 0.68) \cdot 10^{-7}$	$29.98 \pm 3.94$
10.0	11.0	$(6.38 \pm 0.58) \cdot 10^{-6}$	$738 \pm 108$	$4.11 \pm 0.18$	$(4.38 \pm 0.58) \cdot 10^{-7}$	$60.01 \pm 9.61$
11.0	12.0	$(5.40 \pm 0.42) \cdot 10^{-6}$	$572 \pm 79$	$4.18 \pm 0.21$	$(3.21 \pm 0.42) \cdot 10^{-7}$	$35.78 \pm 4.54$
12.0	13.0	$(6.26 \pm 0.60) \cdot 10^{-6}$	$498 \pm 71$	$4.09 \pm 0.20$	$(6.96 \pm 0.60) \cdot 10^{-7}$	$73.11 \pm 10.11$
13.0	14.0	$(6.56 \pm 0.42) \cdot 10^{-6}$	$520 \pm 55$	$4.23 \pm 0.18$	$(3.12 \pm 0.42) \cdot 10^{-7}$	$37.28 \pm 5.62$
14.0	15.0	$(4.48 \pm 0.31) \cdot 10^{-6}$	$310 \pm 46$	$3.67 \pm 0.13$	$(1.33 \pm 0.31) \cdot 10^{-7}$	$21.56 \pm 3.78$
15.0	16.0	$(5.14 \pm 0.35) \cdot 10^{-6}$	$288 \pm 34$	$3.65 \pm 0.12$	$(2.13 \pm 0.35) \cdot 10^{-7}$	$31.06 \pm 5.68$
16.0	17.0	$(2.90 \pm 0.23) \cdot 10^{-6}$	$168 \pm 16$	$3.69 \pm 0.16$	...	...
17.0	18.0	$(2.48 \pm 0.21) \cdot 10^{-6}$	$175 \pm 21$	$3.52 \pm 0.14$	...	...
18.0	19.0	$(1.75 \pm 0.20) \cdot 10^{-6}$	$147 \pm 20$	$3.68 \pm 0.22$	...	...
19.0	20.0	$(2.03 \pm 0.19) \cdot 10^{-6}$	$123 \pm 18$	$3.24 \pm 0.11$	...	...
20.0	21.0	$(1.77 \pm 0.18) \cdot 10^{-6}$	$122 \pm 18$	$3.33 \pm 0.13$	...	...
21.0	22.0	$(1.42 \pm 0.19) \cdot 10^{-6}$	$148 \pm 23$	$3.77 \pm 0.28$	...	...
22.0	23.0	$(1.30 \pm 0.17) \cdot 10^{-6}$	$127 \pm 23$	$3.43 \pm 0.18$	...	...
23.0	24.0	$(1.10 \pm 0.16) \cdot 10^{-6}$	$87 \pm 20$	$3.20 \pm 0.16$	...	...
24.0	25.0	$(6.91 \pm 1.65) \cdot 10^{-7}$	$105 \pm 28$	$3.64 \pm 0.44$	...	...
25.0	26.0	$(9.28 \pm 1.44) \cdot 10^{-7}$	$139 \pm 37$	$3.35 \pm 0.19$	...	...
26.0	27.0	$(6.06 \pm 1.34) \cdot 10^{-7}$	$152 \pm 44$	$3.86 \pm 0.48$	...	...
27.0	28.0	$(7.34 \pm 1.39) \cdot 10^{-7}$	$126 \pm 44$	$3.27 \pm 0.22$	...	...

<sup>a</sup> fixed

<sup>b</sup> synchrotron energy flux

<sup>c</sup> synchrotron  $\nu F_{\nu}$  peak

<sup>d</sup>  $e^{-}$  spectral index

**Table 2**  
Results of the time-resolved spectral analysis of LAT data (100 MeV - 10 GeV) where TS is the value of the Test Statistic.

$T_{\text{start}}$ [s]	$T_{\text{stop}}$ [s]	TS	$\gamma_{\text{ph}}$	$F_{\text{E}}$ [erg s $^{-1}$ cm $^{-2}$ ]
13.3	23.7	26.3	$-2.9 \pm 0.7$	$(7.4 \pm 3.5) \times 10^{-8}$
23.7	75.0	26.8	$-2.1 \pm 0.5$	$(1.6 \pm 1.0) \times 10^{-8}$
75.0	237.1	32.9	$-1.5 \pm 0.4$	$(7.0 \pm 4.5) \times 10^{-9}$
316.2	724.8	7.9	...	$< 2.0 \times 10^{-8}$
3585.8	6446.8	1.8	...	$< 7.7 \times 10^{-10}$
9307.8	10000.0	0.0	...	$< 3.1 \times 10^{-9}$

**Table 3**  
The best-fit parameters of the  $E_{\text{p}}$  evolution fit for each assumed value of  $n_0$  as well as the inferred  $r_{\text{d}}$ .

$n_0$ [cm $^{-3}$ ]	$\Gamma_0$	$\eta$	$q-3$	$g$	$r_{\text{d}}$ [cm]
1	$1125.9^{+16.6}_{-14.3}$	$0.00^{+0.08}_{-0.00}$	$0.17^{+0.01}_{-0.13}$	$1.25^{+0.1}_{-0.1}$	$1.1 \cdot 10^{17}$
10	$844.0^{+12.3}_{-10.9}$	$0.00^{+0.08}_{-0.00}$	$0.17^{+0.02}_{-0.14}$	$1.26^{+0.1}_{-0.11}$	$6.0 \cdot 10^{16}$
100	$632.16^{+7.7}_{-4.5}$	$0.03^{+0.05}_{-0.02}$	$0.17^{+0.05}_{-0.06}$	$1.26^{+0.09}_{-0.11}$	$3.4 \cdot 10^{16}$

for  $g < 1.5$  in Equation 8. Since the obtained value of  $g$  via the fit to the  $E_{\text{p}}$  evolution is not actually measuring the asymptotic behavior of the blast-wave evolution as is intended, we set  $g = 1.6$  in Equation 8 corresponding to a nearly adiabatic blast-wave motivated by the low magnetic fields measured via the spectra and late time XRT observations (see Section 5.1 for full details). This choice of  $g$  does not affect the other parameters in the fit as  $g$  only modifies the late time evolution of  $E_{\text{p}}$  (see Figure 1).

The analytic model given by Equation 7 and Equation 8 is consistent with the data up to a scale factor of 9 which can easily be due to insufficient knowledge of all intrinsic parameters, on the simplified evolution law for the flux, and on the assumed value of  $g$ . It is pertinent to note that the parameters used in the  $P_{\text{p}}(t)$  prediction come from the fitted  $E_{\text{p}}$  evolution alone. In addition, the predicted  $P_{\text{p}}(t)$  is independent of the observed flux values in the data. The close agreement between the predicted and measured  $P_{\text{p}}(t)$  values is evidence that the

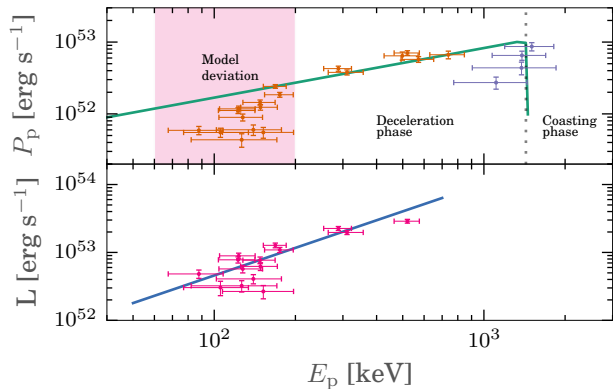


**Figure 6.** The  $P_p - E_p$  plane of GRB 141028A (top) where  $P_p$  is the  $\nu F_\nu$  flux calculated at  $E_p$ . The predicted evolution (green) is produced by substituting the recovered parameters of the  $E_p$  evolution fit into Equation 7. The flux given by Equation 7 is scaled by a factor of 9 to match the data. At late times (pink region), the observed flux decays faster than the model predicts. The decay phase synchrotron HIC (blue) (bottom). The fitted value of the slope is  $\zeta = 1.33 \pm 0.22$ . The decay phase is selected as the portion of the lightcurve that monotonically decreases with time i.e. from 10-27 s.

observed flux at the peak and the observed  $\nu F_\nu$  peak energy are linked in a manner predicted by the external shock model. We do note the deviation from the predicted curve at late times. This therefore provides strong evidence that these two independent quantities are linked in a manner predicted by the external shock model.

#### 4.3. The Luminosity - $E_p$ plane

The commonly observed correlation in the decay phase of many GRB pulses between luminosity and  $E_p$  in the form,

$$L \propto E_p^\zeta, \quad (9)$$

sometimes referred to as the hardness-intensity correlation (HIC) (Golenetskii et al. 1983), is potentially another clue to the radiation mechanism responsible for the observed emission. It is quite simple to relate the luminosity and  $\nu F_\nu$  peak energy of many common radiation mechanisms analytically. However, the spread in HIC power law slopes observed across many GRBs is difficult to explain with one mechanism (Borgonovo & Ryde 2001). However, single pulse GRBs fit with a synchrotron photon model have been found to have HIC power law slopes of  $\sim 1.5$  without much spread (Burgess et al. 2014b).

In Dermer (2004), an analytic form for the HIC resulting from synchrotron emission is derived and parameterized to account for various effects including expansion geometry, magnetic flux-freezing, and radiative regime. Following this derivation, we can make the following predictions for the evolution of the important quantities in determining the relationship between  $L$  and  $E_p$  during the deceleration phase of a blast-wave. We have  $x \propto t^{1/(2g+1)}$ ,  $\Gamma \propto t^{-g/(2g+1)}$ ,  $E_p \propto \Gamma B \gamma_{\min}^2$ , and  $L \propto \Gamma^2 B^2 \gamma_{\min}^2$ . Here  $\gamma_{\min}$  is the minimum electron energy in an assumed shock accelerated power law distribution (though the result is insensitive to the fact that we assume a power law) and  $B$  is the strength of the magnetic field. There are two regimes of cooling for elec-

trons: fast and slow (Sari et al. 1998). Each regime can be characterized by how  $\gamma_{\min}$  evolves with time such that

$$\gamma_{\min} \propto \begin{cases} \Gamma^4 \propto t^{-4g/(2g+1)} & \text{slow cooling} \\ (x\Gamma)^{-1} \propto t^{-2g/(2g+1)} & \text{fast cooling} \end{cases} \quad (10)$$

Since  $L \propto B\Gamma E_p$ , we can write

$$L \propto \begin{cases} E_p^{3/2} & \text{slow cooling} \\ E_p^{1+g} & \text{fast cooling} \end{cases} \quad (11)$$

When fitting the  $L - E_p$  data in the decay phase (10-27 s) we find  $\zeta = 1.33 \pm 0.22$  (see Figure 6). This is closer to the value expected for the slow-cooling regime which falls in line with the use of slow-cooling synchrotron to fit the time-resolved spectra. An a posteriori justification for the use of slow-cooling synchrotron to fit the spectra is discussed in Section 5.1.

#### 4.4. The photosphere

We interpret the observed thermal component in the framework of photospheric emission, i.e., when the outflow becomes transparent at a radius  $\sim 10^{10} - 10^{12}$  cm, i.e., much below  $r_d$ . Because of highly relativistic motion, the observed time delay between photons from the photosphere and those from the external shock is small. As the thermal component is not dominant, the errors in the calculation of outflow parameters derived in Pe'er et al. (2007) are large and we therefore did not use this formalism herein.

We note that the blackbody is not statistically significant (below 3- $\sigma$  confidence level) in the first five seconds after trigger. However, photons from the photosphere are expected to arrive slightly before synchrotron photons. The delay between the photospheric photons and those at the peak of the external shock light curve can be estimated as  $(r_d - r_{\text{ph}})/c\Gamma_0 \simeq 9.5$  s corresponding roughly  $t_d$ . Thus, we added five seconds to the duration of the photospheric emission. The identification of the photospheric emission can give important constraints. First, the duration of the photospheric component ( $\Delta t_{\text{ph}}$ ) sets the width of the expanding outflow ( $W$ ) at the photosphere (see Bégué et al. 2013; Bégué & Iyyani 2014; Vereshchagin 2014),

$$\frac{\Delta t_{\text{ph}}}{1+z} = \frac{R_{\text{ph}}}{2\Gamma_0^2 c} + \frac{W}{c} + \frac{R_{\text{ph}}}{2\Gamma_0^2 c} \quad (12)$$

where the first term accounts for the expansion time of the outflow up to the photosphere, the second term is the light-crossing time of the outflow and the last term is the angular timescale at the photosphere. For the observed duration at hand and for the Lorentz factor values expected in GRB physics, the second term in the right-hand side of the equation dominates. It implies  $W \sim c\Delta t_{\text{ph}}/(1+z) \sim 1.35 \cdot 10^{11}$  cm.

As the width  $W$ , the Lorentz factor  $\Gamma$  and the total energy of the blast wave are constrained, the state of the reverse shock can be a posteriori studied. Following the discussion in Dermer & Menon (2009), we define

$$\xi \sim \frac{54}{\left(\frac{\Gamma}{300}\right)^{4/3} W_8^{1/2}} \left(\frac{E_{52}}{n_0}\right)^{1/6}, \quad (13)$$



such that  $x_{\text{NR}} = \xi r_{\text{d}}$  is the radius at which the reverse shock becomes relativistic. We find  $\xi = 0.8$  which implies that the reverse shock crosses the expanding outflow while it is only mildly relativistic. This justifies the use of Equation 3 in our treatment. We note the value of  $\xi$  is the same for each combination of  $\Gamma_0$  and  $n_0$  (see Table 4).

## 5. DISCUSSION

### 5.1. Compatibility with the Late-time X-ray/optical Emission

Under the assumption of an external shock in the prompt phase, the afterglow is produced by the same process (that is the deceleration of a blast wave by the CBM), and we do not expect any break in the light curve, as already seen in several GRBs observed by *Swift* (Zhang et al. 2006). Unfortunately, the XRT observations only cover a short time range beginning a few  $\sim 10^4$  s after the prompt emission (See Figure 7). At most, we can say that XRT late time observations are compatible with the emission from a decelerating blast-wave in the semi-radiative regime, i.e., a region between  $1.5 < g < 3$ .

In addition, combining observations by XRT and Chandra, displayed in Figure 7, a break can be identified in the light curve. The exact time of the break is unconstrained but it ranges from  $10^5 \text{ s} < t_{\text{b}} < 4.3 \cdot 10^5 \text{ s}$ . Identifying the break as a jet break, the jet opening angle can be estimated to be (Ghirlanda et al. 2004)

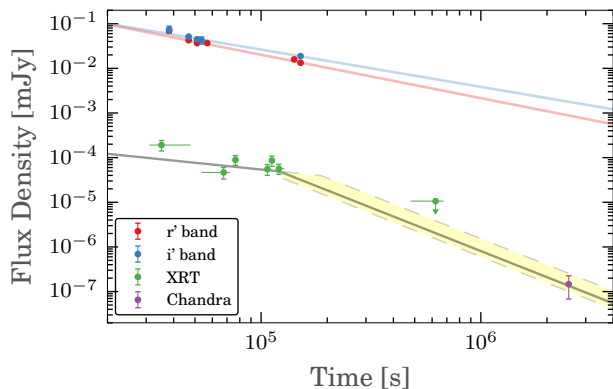


**Figure 7.** The X-ray and optical afterglow of GRB 141028A. A power law fit best describes the optical data while a broken power law fit, indicative of a jet break, best describes the X-ray data. The *yellow* shaded region indicates the 90% uncertainty in the break time due to the sparse sampling of data prior to the Chandra follow-up observation.

$$\theta_j = 0.161 \left( \frac{t_{\text{b}}}{1+z} \right)^{3/8} \left( \frac{\eta_{\gamma} n_0}{E_{\gamma, \text{iso}, 52}} \right)^{1/8} \quad (14)$$

where  $t_{\text{b}}$  is the break time in days and  $\eta_{\gamma}$  is the radiative efficiency taken to be 0.1 corresponding to our assumption of  $E_0 = 10^{55}$  erg. Thus, the opening angle ranges from  $2.65^\circ < \theta_j < 8.15^\circ$ , when considering the fitted parameters obtained in Section 4.1. Therefore, the radiative energy budget of the burst is considerably reduced to few  $\sim 10^{51}$  erg (see Table 5).

Finally, additional constraints can be obtained from simultaneous optical and X-ray observations at around

**Table 4**

Values of  $\epsilon_{\text{B}}$  from the afterglow and  $E_{\text{p}}$  assuming different values of  $n_0$  as well as the location of the relativistic reverse shock ( $\xi$ ).

$n_0$	$\Gamma_0$	$\epsilon_{\text{B}}$ via $\nu_{\text{c}}$	$\epsilon_{\text{B}}$ via $E_{\text{p}}$	$\xi$
1	1125.9	$< 1.2 \cdot 10^{-3}$	$\sim 2.9 \cdot 10^{-9}$	0.8
10	884.0	$< 2.7 \cdot 10^{-4}$	$\sim 2.9 \cdot 10^{-9}$	0.8
100	632.2	$< 5.7 \cdot 10^{-5}$	$\sim 2.9 \cdot 10^{-9}$	0.8

**Table 5**

Corrected Emitted Burst Energy ( $E_{\text{cor}}$ )

$n_0$ [ $\text{cm}^{-3}$ ]	$t_{\text{b}}$ (s)	$\theta_j$ (degrees)	$E_{\text{cor}}$ (erg)
1	$1 \cdot 10^5$	2.65	$1.0 \cdot 10^{51}$
	$4.3 \cdot 10^5$	4.58	$2.9 \cdot 10^{51}$
10	$1 \cdot 10^5$	3.53	$1.7 \cdot 10^{51}$
	$4.3 \cdot 10^5$	6.1	$5.2 \cdot 10^{51}$
100	$1 \cdot 10^5$	4.71	$3.1 \cdot 10^{51}$
	$4.3 \cdot 10^5$	8.15	$9.2 \cdot 10^{51}$

50 ks after the trigger. The spectrum is consistent with a single power-law of index  $\beta = 1.29 \pm 0.07$ . Therefore, we can deduce that the cooling frequency is above the XRT frequency:  $\nu_{\text{c}} > \nu_{\text{XRT}}$ . From the expansion of a blast-wave in a constant density CBM,  $\nu_{\text{c}}$  can be estimated as (Panaitescu & Kumar 2000a)

$$\nu_{\text{c}} = 3.7 \cdot 10^{16} E_{53}^{-1/2} n_0^{-1} (Y+1)^{-2} \epsilon_{\text{B}, -2}^{-3/2} T_{\text{d}}^{-1/2} \text{ Hz}, \quad (15)$$

where  $\epsilon_{\text{B}}$  parameterizes the magnetic field in the shocked ISM,  $T_{\text{d}}$  is the time in days and  $Y$  is the Compton parameter, that we chose to be zero for simplicity. This leads to an upper limit  $\epsilon_{\text{B}} < 2.3 \cdot 10^{-5}$  taking  $T_{\text{d}} = 1$  day and assuming  $n_0 = 100$  and  $E_{53} = 100$  which implies  $\Gamma_0 = 632$  (see however, Table 4 for values corresponding to different parameter choices).

Also, this value can be cross-checked by considering the peak energy in the first seconds of the prompt phase, which can be evaluated as:

$$E_{\text{p}} \simeq \frac{\sqrt{32\pi\epsilon_{\text{B}} m_{\text{p}} c^2 n_0 \Gamma^2}}{B_{\text{crit}}} \Gamma \gamma_{\text{min}}^2 \quad (16)$$

where  $B_{\text{crit}} = 4.414 \cdot 10^{13} \text{ G}$  is the critical magnetic field,  $\kappa$  parameterizes the minimum Lorentz factor  $\gamma_{\text{min}}$  of the accelerated electrons such that  $\gamma_{\text{min}} = \kappa \Gamma (m_{\text{p}}/m_{\text{e}})$ ,  $m_{\text{e}}$  is the mass of an electron, and  $E_{\text{p}}$  is given in units of the mass of an electron. Using  $E_{\text{p}} \sim 1.3 \text{ MeV}$  and  $n_0 = 100$  as obtained from the data, and assuming  $\kappa = 1$  gives  $\epsilon_{\text{B}} \sim 3.0 \cdot 10^{-9}$  (see also Table 4). This value is consistent with the upper limit obtained from the late afterglow<sup>9</sup>.

Finally, the cooling time of an electron with Lorentz factor  $\gamma_{\text{min}}$  can be compared to the expansion time of the blast-wave at the observed luminosity peak which

<sup>9</sup> However we note that this value is very sensitive to  $\kappa$  which is fairly unconstrained: as an example, with  $\kappa = 0.1$ , it becomes  $\epsilon_{\text{B}} \sim 2.8 \cdot 10^{-9}$ , incompatible with the upper limit obtained from the afterglow.



is on the order of the  $t_d$ . We find that they are comparable, leading to efficient energy extraction from the electrons, without drastically changing the electron distribution function, *i.e.*, creating an additional power law over several orders of magnitude at low-energy characteristic of fast-cooled (or completely cooled) electrons.

### 5.2. LAT late time GeV emission

*Fermi* LAT observed a GeV component over the duration of  $10 - 10^3$  s. Unfortunately, there were no simultaneous observations at other wavelengths from which a broadband spectrum could be obtained. Nevertheless, we can use the analytic flux evolution derived in Dermer et al. (1999) to check if the observed LAT fluxes are compatible with the model. We must first address a few caveats: the analytic model assumes no synchrotron self-Compton (SSC) emission and the fluxes are sensitive to our lack of knowledge about the total burst energy (which we assume to be  $10^{55}$  erg for the purpose of calculation) as well as the degeneracies in the recovered parameters from the  $E_p$  evolution fit.

In the past years, a debate concerning the origin of the late time (few seconds after the trigger) high-energy LAT emission has taken place, opposing a synchrotron mechanism (Kumar & Barniol Duran 2009, 2010), SSC (Panaitescu & Kumar 2000b), and pair-loading of the CBM (Beloborodov 2005) as the possible candidates for this emission. First, we can assess the SSC component, and show that with the parameters at hand from the prompt emission the SSC flux in the LAT bandpass is much less than the synchrotron flux. We can constrain the SSC flux in the LAT bandpass by following the discussion in Beniamini & Piran (2013) (see Appendix B for further details). Via Equation B12, the ratio of SSC flux to synchrotron flux in the LAT bandpass ( $\mathcal{F}_{\text{SSC}}$ ) can be computed by substituting values derived in Section 5.1 to yield  $\mathcal{F}_{\text{SSC}} \simeq 10^{-8}$ . The numerical result shows that the SSC flux in the LAT band is much less than the synchrotron flux. However, the computation *relies* on the assumption that electrons are fast cooled either by synchrotron or by inverse Compton of the produced synchrotron photons, that is to say that all the energy is emitted by one or the other mechanism. It comes with two consequences:

1. the Compton parameter *is* an upper limit as shown in Sari et al. (1996). Therefore the result of Eq.(B12) is only an upper limit,
2. as a result of the assumption of fast cooling, the electron distribution function extends to small Lorentz factors. These electrons are not in the Klein-Nishina regime and can efficiently upscattered synchrotron photon in the LAT band. However, we found that electrons with Lorentz factor  $\gamma_{\text{min}}$  are not strongly cooled over a dynamical time. Therefore the electron distribution function does not extend substantially below  $\gamma_{\text{min}}$ , reducing the inverse Compton flux.

We now consider that the GeV emission is the result of synchrotron emission from the same forward-shock responsible for the lower energy prompt phase. Using the analytic estimate for the blast-wave evolution, we esti-

mate the expected flux of the synchrotron emitting blast-wave and compare it to the integrated (100 MeV - 10 GeV) LAT energy flux ( $F_E$ ) by integrating Equation 1 from Dermer et al. (1999) across the LAT bandpass (see Figure 8). Because of our lack of knowledge about the intrinsic total energy of the blast-wave and the degeneracies in the fit parameters ( $q$ ,  $n_0$ ), we vary the parameters across a broad range and find that the model gives consistent limits within an order of magnitude. We also note that this model is simple and will not be as accurate as a full numerical solution. Additionally, using the power-law electron index ( $p$ ) found from GBM+LLE synchrotron fits, we compute the synchrotron photon indices via the transformation  $\gamma_{\text{ph}} = -(p + 1)/2$  and compare them with the photon indices found in the LAT alone (Figure 9). There is a clear evolution of the synchrotron photon index increasing that smoothly transitions to the indices observed by the LAT.

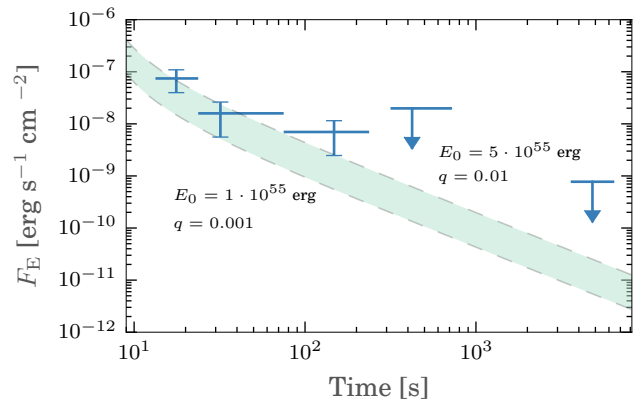


**Figure 8.** The LAT GeV integrated energy fluxes (100 MeV - 10 GeV) are compared with a range of expected fluxes from the analytic model of Dermer et al. (1999) that includes only synchrotron emission. Suitable agreement can be found for a valid range of assumed blast-wave parameters.

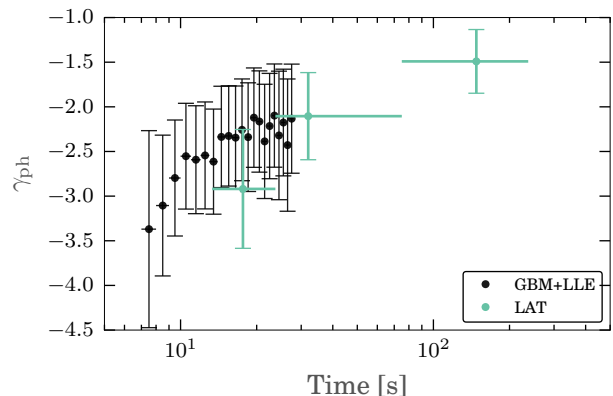


**Figure 9.** The photon indices from the GBM+LLE fits and LAT fits. A clear evolution is seen into the LAT band pass with the indices all in line with what could be expected from synchrotron-emitting high-energy electrons accelerated into a power law momentum-distribution.

Therefore, we conclude that the high energy emission from the LAT is compatible with synchrotron emission

alone, and does not require an additional mechanism. It was proposed by Kumar & Barniol Duran (2009, 2010), in which the prompt MeV phase is assumed to be the result of an unspecified mechanism, that the GeV LAT emission arises from a separate external shock with a synchrotron peak on the order of a few 100 MeV. Conditions on the density and the magnetic field are then derived such that this external shock is not more luminous than the prompt emission in the sub-MeV band. However, for GRB *141028A* we show that the entire emission can be explained by synchrotron emission with an MeV peak energy from a single forward shock without fine-tuning of the parameters, i.e., both the MeV and the delayed GeV can be explained self-consistently by an external shock.

### 5.3. Summary of Prompt Phase

In this section, we concisely summarize the novel approach we have employed to test the external shock model in the prompt phase. Almost as important as the observed  $E_p$  evolution is the fact that we can fit the spectrum with a physical slow-cooling synchrotron model. Even though it is possible to fit a physical synchrotron model to the spectra (as opposed to an empirical Band function from which the comparison to physical models must be inferred and can lead to problems as shown in Burgess et al. (2014a)), it must be shown that the photon model is sound, i.e., that the dynamical evolution can lead to slow-cooling synchrotron emission. In Section 5.1, we confirmed that both the afterglow and prompt phase are consistent with slow-cooling emission.

The evolution of  $E_p$  in time can be fit with the analytic prediction of Dermer et al. (1999). While the blast-wave appears to be transitioning to the asymptotic limits, ( $g < 1.5$ ) we tentatively conclude that it is evolving towards an adiabatic regime. Full temporal coverage of the flux and spectra through the late time evolution will help to resolve this issue. Unfortunately, few single pulsed GRBs have been observed with such a temporal and wavelength coverage. This unique opportunity presents itself only due to the current multi-mission capabilities and begs for continued multi-wavelength coverage.

If we take the fitted parameters of the  $E_p$  evolution fit, we can predict the evolution of the  $P_p - E_p$  plane which is consistent with the data in both the rise and decay phase of the pulse. The HIC of the prompt decay phase of the synchrotron luminosity is consistent with what would be expected from slow-cooling synchrotron in a decelerating external shock.

We use the observation of the photospheric component to estimate both the width of the blast-wave as well as when the relativistic reverse shock crosses the forward shock. From our calculations, the reverse shock will have very little impact on the evolution of the forward shock and we therefore neglect it.

## 6. CONCLUSION

In this article, we have shown that the prompt phase of GRB *141028A* is consistent with originating from an external shock that emits synchrotron radiation from an electron distribution that did not have enough time to cool completely (slow-cooled). Combining the results of the  $E_p$  evolution fits with the other clues from the data, an external shock origin of GRB *141028A* is a very likely scenario. Not only do we find that the prompt emission is

explained by synchrotron emission from a forward shock, but we find clues for a late time high-energy emission resulting from the extension of this synchrotron emission rather than an SSC component. We want to stress that in this scenario the delineation between “prompt” and “afterglow” is superfluous as the early and late time emission both originate from the same mechanism. We are currently applying this analysis to other long, single pulse GRBs and find that they too have their  $\nu F_\nu$  peak and  $P_p(t)$  which evolved consistently with the predictions of an external shock. These results will be presented in a forthcoming publication.

We propose that external shocks are still a viable candidate to explain the prompt dynamics of GRBs. However, the most likely scenario is that they are a subset of multiple dynamical frameworks including internal shocks that further subdivide into categories based on opacity and/or magnetic content of the outflow. We note that this is not an entirely new idea. Panaitescu & Mészáros (1998) numerically investigated the parameter space of the external shock model and proposed that smooth, single-pulsed (and possibly multi-pulsed) GRBs can belong to a subclass of GRBs that are the results of external shocks. We have now shown this quantitatively by applying the model to the data.

The analysis of individual GRBs is crucial to identifying what is likely a host of different emission mechanisms. For example, GRB *090902B* exhibits dynamics and spectra that are consistent with subphotospheric dissipation (Ryde et al. 2010). The fact that both external shocks and photospheric emission are observationally viable candidates for explaining GRB emission implies that we should use caution when trying to apply one mechanism as an explanation for all GRBs based of properties from catalogs and should instead focus on how to relate the different emission mechanisms into a unified framework.

The authors are very grateful for insightful discussions with Chuck Dermer, Peter Mészáros, Gregory Vereshchagin and Peter Veres that helped to improve the manuscript. This work made use of data supplied by the UK Swift Science Data Centre at the University of Leicester, data obtained from the Chandra Data Archive, and software provided by the Chandra X-ray Center (CXC). JLR and AC acknowledge support for this work from NASA through Chandra Award Number GO4-15073Z issued by the Chandra X-ray Observatory Center under contract NAS8-03060.

The *Fermi* LAT Collaboration acknowledges generous ongoing support from a number of agencies and institutes that have supported both the development and the operation of the LAT as well as scientific data analysis. These include the National Aeronautics and Space Administration and the Department of Energy in the United States, the Commissariat à l’Energie Atomique and the Centre National de la Recherche Scientifique / Institut National de Physique Nucléaire et de Physique des Particules in France, the Agenzia Spaziale Italiana and the Istituto Nazionale di Fisica Nucleare in Italy, the Ministry of Education, Culture, Sports, Science and Technology (MEXT), High Energy Accelerator Research Organization (KEK) and Japan Aerospace Exploration Agency

(JAXA) in Japan, and the K. A. Wallenberg Foundation, the Swedish Research Council and the Swedish National Space Board in Sweden.

Additional support for science analysis during the operations phase is gratefully acknowledged from the Istituto Nazionale di Astrofisica in Italy and the Centre National d'Études Spatiales in France.

This research made use of `Astropy`, a community-developed core Python package for Astronomy (`Astropy` Collaboration et al. 2013) as well `Matplotlib`, an open source Python graphics environment (Hunter 2007). We also thank the developer of `pymultinest` for enabling the use of `MULTINEST` in the Python environment (Buchner et al. 2014). All computational work was performed with the Mac OS X operating system via the Intel Core *i7* architecture.

#### REFERENCES

- Ackermann, M., Ajello, M., Allafort, A., et al. 2012, *ApJ*, 745, 144  
 Ackermann, M., Ajello, M., Asano, K., et al. 2013, *ApJS*, 209, 11  
 Ajello, M., Albert, A., Allafort, A., et al. 2014, *ApJ*, 789, 20  
 Astropy Collaboration, Robitaille, T. P., Tollerud, E. J., et al. 2013, *A&A*, 558, A33  
 Atwood, W. B., Abdo, A. A., Ackermann, M., et al. 2009, *ApJ*, 697, 1071  
 Band, D., Matteson, J., & Ford, L. 1993, *ApJ*, 413, 281  
 Bégué, D., & Iyyani, S. 2014, *ApJ*, 792, 42  
 Bégué, D., Siutsou, I. A., & Vereshchagin, G. V. 2013, *ApJ*, 767, 139  
 Beloborodov, A. M. 2005, *ApJ*  
 Beniamini, P., & Piran, T. 2013, *ApJ*, 769, 69  
 Bissaldi, E., et al. 2014, *GCN Circular*, 16969  
 Blandford, R. D., & McKee, C. F. 1976, *Phys Fluids*, 19, 1130  
 Borgonovo, L., & Ryde, F. 2001, *ApJ*, 548, 770  
 Buchner, J., Georgakakis, A., Nandra, K., et al. 2014, *A&A*, 564, A125  
 Burgess, J. M., Ryde, F., & Yu, H.-F. 2014a, *arXiv*, 7647  
 Burgess, J. M., Preece, R. D., Baring, M. G., et al. 2011, *ApJ*, 741, 24  
 Burgess, J. M., Preece, R. D., Connaughton, V., et al. 2014b, *ApJ*, 784, 17  
 Cavallo, G., & Rees, M. J. 1978, *MNRAS*, 183, 359  
 Cenko, S. B. 2014, *GCN Circular*, 16989  
 Chiang, J., & Dermer, C. D. 1999, *ApJ*, 512, 699  
 Daigne, F., & Mochkovitch, R. 1998, *MNRAS*, 296, 275  
 de Jager, O. C., Harding, A. K., Michelson, P. F., et al. 1996, *ApJ*, 457, 253  
 Dermer, C. D. 2004, *ApJ*, 614, 284  
 Dermer, C. D., Chiang, J., & Böttcher, M. 1999, *ApJ*, 513, 656  
 Dermer, C. D., & Menon, M. 2009, *High Energy Radiation from Black Holes* (Princeton University Press)  
 Dermer, C. D., & Mitman, K. E. 1999, *ApJL*, 513, L5  
 Drenkhahn, G., & Spruit, H. C. 2002, *A&A*, 391, 1141  
 Evans, P. A., Beardmore, A. P., Page, K. L., et al. 2007, *A&A*, 469, 379  
 —. 2009, *MNRAS*, 397, 1177  
 Feroz, F., Hobson, M. P., & Bridges, M. 2009, *MNRAS*, 398, 1601  
 Gao, H., Zhang, B.-B., & Zhang, B. 2012, *ApJ*, 748, 134  
 Gehrels, N., Chincarini, G., Giommi, P., et al. 2004, *ApJ*, 611, 1005  
 Ghirlanda, G., Ghisellini, G., & Lazzati, D. 2004, *ApJ*, 616, 331  
 Golenetskii, S. V., Mazets, E. P., Aptekar, R. L., & Ilinskii, V. N. 1983, *Nature* (ISSN 0028-0836), 306, 451  
 Golkhou, V. Z., & Butler, N. R. 2014, *ApJ*, 787, 90  
 Golkhou, V. Z., Butler, N. R., & Littlejohns, O. M. 2015, *arXiv*, 5948  
 Hogg, D. W., Baldry, I. K., Blanton, M. R., & Eisenstein, D. J. 2002, *arXiv*, 10394  
 Hunter, J. D. 2007, *Computing In Science & Engineering*, 9, 90  
 Kann, A. 2014, *GCN Circular*, 16977  
 Kennea, J. A. 2014, *GCN Circular*, 16978  
 Kobayashi, S., Piran, T., & Sari, R. 1997, *ApJ*, 490, 92  
 Kopac, D. 2014, *GCN Circular*, 16985  
 Kumar, P., & Barniol Duran, R. 2009, *MNRAS*, 400, L75  
 —. 2010, *MNRAS*, 409, 226  
 Lemoine, M., Li, Z., & Wang, X.-Y. 2013, *MNRAS*, 435, 3009  
 Malesani, D. 2014, *GCN Circular*, 16983  
 Mattox, J. R., et al. 1996, *ApJ*, 461, 396  
 Meegan, C., Lichti, G., Bhat, P. N., et al. 2009, *ApJ*, 702, 791  
 Mészáros, P., & Rees, M. J. 1993, *ApJ*, 405, 278  
 Nolan, P. L., Abdo, A. A., Ackermann, M., et al. 2012, *VizieR Online Data Catalog*, 219, 90031  
 Panaitescu, A., & Kumar, P. 2000a, *ApJ*, 543, 66  
 —. 2000b, *ApJ*, 543, 66  
 Panaitescu, A., & Mészáros, P. 1998, *ApJ*, 492, 683  
 Pe'er, A., Meszaros, P., & Rees, M. J. 2005, *ApJ*, 635, 476  
 Pe'er, A., Ryde, F., Wijers, R. A. M. J., Mészáros, P., & Rees, M. J. 2007, *ApJL*, 664, L1  
 Protassov, R., van Dyk, D. A., Connors, A., Kashyap, V. L., & Siemiginowska, A. 2002, *ApJ*, 571, 545  
 Rees, M. J., & Mészáros, P. 1992, *MNRAS*, 258, 41P  
 —. 1994, *arXiv*, L93  
 Roberts, O. 2014, *GCN Circular*, 16971  
 Ryde, F., Axelsson, M., Zhang, B. B., et al. 2010, *ApJL*, 709, L172  
 Santana, R., Barniol Duran, R., & Kumar, P. 2014, *ApJ*, 785, 29  
 Sari, R., Narayan, R., & Piran, T. 1996, *ApJ*, 473, 204  
 Sari, R., & Piran, T. 1997, *ApJ*, 485, 270  
 Sari, R., Piran, T., & Narayan, R. 1998, *ApJL*, 497, L17  
 Siegel, M. H., & Paganí, C. 2014, *GCN Circular*, 16979  
 Spruit, H. C., Daigne, F., & Drenkhahn, G. 2001, *A&A*, 369, 694  
 Troja, E. 2014, *GCN Circular*, 16980  
 Vereshchagin, G. V. 2014, *Int. J. Mod. Phys. D*, 23, 1430003  
 Walker, K. C., Schaefer, B. E., & Fenimore, E. E. 2000, *ApJ*, 537, 264  
 Wilks, S. S. 1938, *Ann. Math. Stat.*, 9, 60  
 Zhang, B., Fan, Y. Z., Dyks, J., et al. 2006, *ApJ*, 642, 354  
 Zhang, B., & Yan, H. 2011, *ApJ*, 726, 90

#### APPENDIX

##### LAT ANALYSIS

The model used in the likelihood fit is composed of the Galactic diffuse emission produced by cosmic-ray interaction with gas and radiation fields and the isotropic diffuse emission. In addition, we add all the point sources in the ROI with spectral models and parameters from the 2FGL catalog (Nolan et al. 2012). While the normalization of the Galactic template and the spectral parameters of all the 2FGL sources are frozen to their nominal values, the normalization of the isotropic template is left free to vary in order to absorb statistical fluctuations. The GRB location is fixed, and its spectrum is described by a power law  $dN/dE \propto E^{\gamma_{\text{ph}}}$  with  $\gamma_{\text{ph}}$  the photon index (note that typically  $\gamma_{\text{ph}} < 0$ ). Following the time-resolved analysis described in Ackermann et al. (2013) we split the LAT data in 48 log-spaced time bins from 0.01 to 10000 seconds after the trigger. The logarithmically-spaced binning provides constant-fluence bins when applied to a signal that decreases approximately as  $1/\text{time}$ , such as the extended GRB emissions observed by the LAT. We first merge consecutive time bins in order to have at least 5 counts per bin (corresponding to the number of free parameters in the likelihood model plus 2), and we then perform likelihood analysis. We estimate the significance of the GRB source by evaluating the “Test Statistic” (TS) equal to twice the logarithm of the ratio of the maximum

likelihood value produced with a model including the GRB over the maximum likelihood value of the null hypothesis, i.e., a model that does not include the GRB. The probability distribution function (PDF) of the TS under the null hypothesis is given by the probability that a measured signal is compatible with statistical fluctuations. The PDF in such a source-over-background model cannot, in general, be described by the usual asymptotic distributions expected from Wilks' theorem (Wilks 1938; Protassov et al. 2002). However, it has been verified by dedicated Monte Carlo simulations (Mattox et al. 1996) that the cumulative PDF of the TS in the null hypothesis (i.e., integral of the TS PDF from some TS value to infinity) is approximately equal to a  $\chi^2_{n_{\text{dof}}}/2$  distribution, where  $n_{\text{dof}}$  is the number of degrees of freedom associated with the GRB. The factor of 1/2 in front of the TS PDF formula results from allowing only positive source fluxes.

If the resulting TS value is lower than an arbitrary threshold ( $TS < 10$ ) we merge the corresponding time bin with the next one, and we repeat the likelihood analysis. This step is iterated until one of two conditions is satisfied: 1) we reach the end of a GTI before reaching  $TS = 10$ , in which case we compute the value of the 95% CL upper limit (UL) for the flux evaluated using a photon index of  $-2$ ; 2) we reach  $TS > 10$ , in which case we evaluate the best-fit values of the flux and the spectral index along with their  $1\sigma$  errors.

#### HIGH-ENERGY SSC FRACTION

Following Beniamini & Piran (2013), the SSC and Klein-Nishina peak frequencies are defined respectively as

$$\nu_{\text{min}} = E_{\text{p}} h^{-1} \quad (\text{B1})$$

$$\nu_{\text{SSC}} = \gamma_{\text{min}}^2 \nu_{\text{min}} \quad (\text{B2})$$

$$\nu_{\text{KN}} = \Gamma \gamma_{\text{min}} m_e c^2 h^{-1} \quad (\text{B3})$$

where  $h$  is Planck's constant. The total SSC flux is linked to the total synchrotron flux at the peak ( $F_{\nu_{\text{min}}}^{\text{SYNCH}}$ ) by

$$\frac{F_{\text{SSC}}}{\nu_{\text{min}} F_{\nu_{\text{min}}}^{\text{SYNCH}}} = Y \Lambda_{\text{KN}} \quad (\text{B4})$$

where  $Y$  is the Compton parameter and,

$$\Lambda_{\text{KN}} = \begin{cases} \left( \frac{\nu_{\text{SSC}}}{\nu_{\text{KN}}} \right)^{-1/2} & \frac{\nu_{\text{SSC}}}{\nu_{\text{KN}}} > 1 \\ 1 & \text{otherwise} \end{cases} \quad (\text{B5})$$

In the derivation of the  $Y$  via Sari et al. (1996), the Klein-Nishina correction of the Compton cross-section ( $\sigma_{\text{KN}} \propto \ln(2x)/x$  where  $x$  is the photon energy in the rest frame of the electron in  $m_e c^2$  units) was ignored. Here, in order to estimate  $Y$  we include this correction by considering electrons with Lorentz factor  $\gamma_{\text{min}}$  and their corresponding synchrotron photons. Therefore, we write

$$Y = \left( \frac{\epsilon_e}{\epsilon_B} \right)^{1/2} \cdot \left[ \frac{\ln \left( 2 \frac{\gamma_{\text{min}} h \nu_{\text{min}}}{m_e c^2} \right)}{\gamma_{\text{min}} \frac{h \nu_{\text{min}}}{m_e c^2}} \right]^{1/2} \quad (\text{B6})$$

The total upscattered flux in the LAT bandpass can then be written as

$$\frac{F_{\text{SSC}}^{\text{LAT}}}{\nu_{\text{min}} F_{\nu_{\text{min}}}^{\text{SYNCH}}} = \frac{F_{\text{SSC}}}{\nu_{\text{min}} F_{\nu_{\text{min}}}^{\text{SYNCH}}} \cdot \Lambda_{\text{W}} \quad (\text{B7})$$

where

$$\Lambda_{\text{W}} = \begin{cases} 1 & \min(\nu_{\text{SSC}}, \nu_{\text{KN}}) < \nu_{\text{max}} \\ \left( \frac{\min(\nu_{\text{SSC}}, \nu_{\text{KN}})}{\nu_{\text{max}}} \right)^{-\alpha-2} & \text{otherwise} \end{cases} \quad (\text{B8})$$

Here,  $\alpha$  refers to the low-energy photon index of the Band function which is  $-2/3$  in our case and  $\nu_{\text{max}}$  is the maximum synchrotron frequency corresponding to the maximum Lorentz factor of the accelerated electrons (de Jager et al. 1996):

$$\gamma_{\text{max}} = 4 \cdot 10^7 \left( \frac{B}{1 \text{ G}} \right)^{-1/2} \quad (\text{B9})$$

In order to estimate the synchrotron flux in the LAT band pass, we write

$$F_{\nu}^{\text{SYNCH}} = \left( \frac{\nu}{\nu_{\text{min}}} \right)^{-\frac{s-1}{2}} F_{\nu_{\text{min}}}^{\text{SYNCH}} \quad (\text{B10})$$

where  $s$  is the high-energy electron power law index which we take  $s \equiv 2.5$  for simplicity. Then we can write the fraction of SSC to synchrotron flux in the LAT bandpass as

$$\mathcal{F}_{\text{SSC}} \equiv \frac{F_{\text{SSC}}^{\text{LAT}}}{F_{\text{SYNCH}}^{\text{LAT}}} = \frac{F_{\text{SSC}}^{\text{LAT}}}{\int_{\text{LAT}} d\nu \left(\frac{\nu}{\nu_{\text{min}}}\right)^{-\frac{s-1}{2}} F_{\nu_{\text{min}}^{\text{SYNCH}}}} \quad (\text{B11})$$

This can be further simplified via Equations B4 and B7 to

$$\mathcal{F}_{\text{SSC}} = \frac{\nu_{\text{min}}}{\int_{\text{LAT}} d\nu \left(\frac{\nu}{\nu_{\text{min}}}\right)^{-\frac{s-1}{2}}} \cdot \Lambda_{\text{W}} \cdot \Lambda_{\text{KN}} \cdot Y. \quad (\text{B12})$$

This is in fact an upper limit on the fraction of SSC due to the assumption that electrons radiate all their energy in a dynamical time either by synchrotron *and/or inverse-Compton* and that there is a significant fraction of electrons below  $\gamma_{\text{min}}$ . If either assumption fails (as is true in our analysis) the fraction of SSC emission will be suppressed.